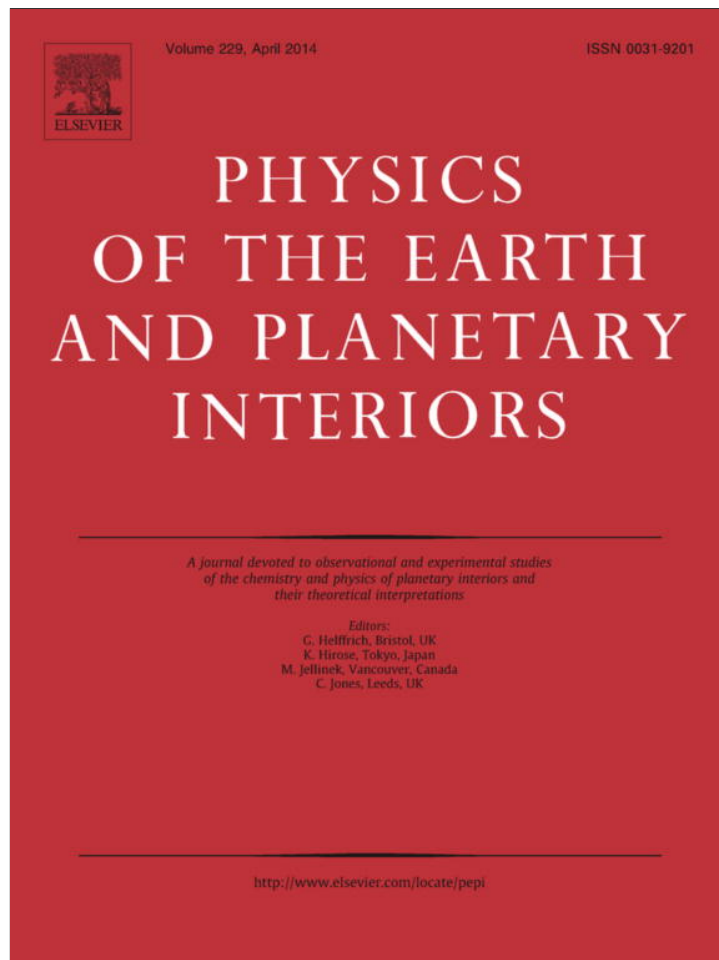


Provided for non-commercial research and education use.
Not for reproduction, distribution or commercial use.



This article appeared in a journal published by Elsevier. The attached copy is furnished to the author for internal non-commercial research and education use, including for instruction at the authors institution and sharing with colleagues.

Other uses, including reproduction and distribution, or selling or licensing copies, or posting to personal, institutional or third party websites are prohibited.

In most cases authors are permitted to post their version of the article (e.g. in Word or Tex form) to their personal website or institutional repository. Authors requiring further information regarding Elsevier's archiving and manuscript policies are encouraged to visit:

<http://www.elsevier.com/authorsrights>



Contents lists available at ScienceDirect

Physics of the Earth and Planetary Interiors

journal homepage: www.elsevier.com/locate/pepi

Source process and tectonic implication of the January 20, 2007 Odaesan earthquake, South Korea

Ali K. Abdel-Fattah^{a,c,*}, K.Y. Kim^b, M.S. Fnais^a, A.M. Al-Amri^a^a King Saud University, Faculty of Science, Geology and Geophysics Department, Riyadh, Saudi Arabia^b Department of Geophysics, Kangwon National University, Chuncheon, Republic of Korea^c Department of Seismology, National Research Institute of Astronomy and Geophysics, 11421 Helwan, Cairo, Egypt

ARTICLE INFO

Article history:

Received 22 August 2013

Received in revised form 8 January 2014

Accepted 8 January 2014

Available online 18 January 2014

Edited by Vernon F. Cormier

Keywords:

Focal depth

Grid search

Source mechanism

Waveform inversion

South Korea

ABSTRACT

The source process for the 20th of January 2007, Mw 4.5 Odaesan earthquake in South Korea is investigated in the low- and high-frequency bands, using velocity and acceleration waveform data recorded by the Korea Meteorological Administration Seismographic Network at distances less than 70 km from the epicenter. Synthetic Green functions are adopted for the low-frequency band of 0.1–0.3 Hz by using the wave-number integration technique and the one dimensional velocity model beneath the epicentral area. An iterative technique was performed by a grid search across the strike, dip, rake, and focal depth of rupture nucleation parameters to find the best-fit double-couple mechanism. To resolve the nodal plane ambiguity, the spatiotemporal slip distribution on the fault surface was recovered using a non-negative least-square algorithm for each set of the grid-searched parameters. The focal depth of 10 km was determined through the grid search for depths in the range of 6–14 km. The best-fit double-couple mechanism obtained from the finite-source model indicates a vertical strike-slip faulting mechanism. The NW faulting plane gives comparatively smaller root-mean-squares (RMS) error than its auxiliary plane. Slip pattern event provides simple source process due to the effect of Low-frequency that acted as a point source model. Three empirical Green functions are adopted to investigate the source process in the high-frequency band. A set of slip models was recovered on both nodal planes of the focal mechanism with various rupture velocities in the range of 2.0–4.0 km/s. Although there is a small difference between the RMS errors produced by the two orthogonal nodal planes, the SW dipping plane gives a smaller RMS error than its auxiliary plane. The slip distribution is relatively assessable by the oblique pattern recovered around the hypocenter in the high-frequency analysis; indicating a complex rupture scenario for such moderate-sized earthquake, similar to those reported for large earthquakes.

© 2014 Elsevier B.V. All rights reserved.

1. Introduction

Southern part of the Korean Peninsula (SKP) is tectonically controlled by the relative motions between the Pacific, Philippine and Eurasian plates (Fig. 1; Molnar and Tapponnier, 1975; Kato et al., 1998; Kogan et al., 2000). These relative motions might be responsible for the occurrence of intraplate earthquakes in the SKP with strike-slip faulting mechanisms and minor dip- or reverse-slip components (June, 1990; Kim, 1993; Kim et al., 2004). Park et al. (2007) indicated that strike-slip faulting with a reverse-slip component is the dominant mechanism in the SKP and suggested that NNW- to NE-striking faults are most likely to generate earthquakes in the SKP. The SKP is characterized by relatively low seismic activ-

ities with small- to moderate-size earthquakes that do not produce surface ruptures and relatively few aftershocks following the main-shock events. Moreover, the seismicity is randomly distributed and no tectonic trends are clearly traced. Therefore, identification of active fault planes is generally a difficult issue in this region.

Since local tectonics and occurrence of intraplate earthquakes are not understood well in the Korean peninsula, it is important to depict in detail the rupture processes of small- to moderate-size earthquakes. This may help to identify the active faults in this region. At 11:56:53.48 on January 20, 2007 an Mw 4.5 earthquake struck Gangwon province of South Korea (Fig. 2). The earthquake felt widely over the SKP attracted public attention although no damage was reported. Four aftershocks with magnitudes in the range of 2.5–2.8 occurred, three on the same day, with the fourth and smallest occurring one day later.

In the present study, we aim to investigate the spatial and temporal slip distribution of the Odaesan earthquake in both low- and

* Corresponding author at: King Saud University, Faculty of Science, Geology and Geophysics Department, Riyadh, Saudi Arabia. Tel.: +20 507433140.

E-mail addresses: ali_kamel100@yahoo.co.uk, ali_kamel@yahoo.com (A.K. Abdel-Fattah).

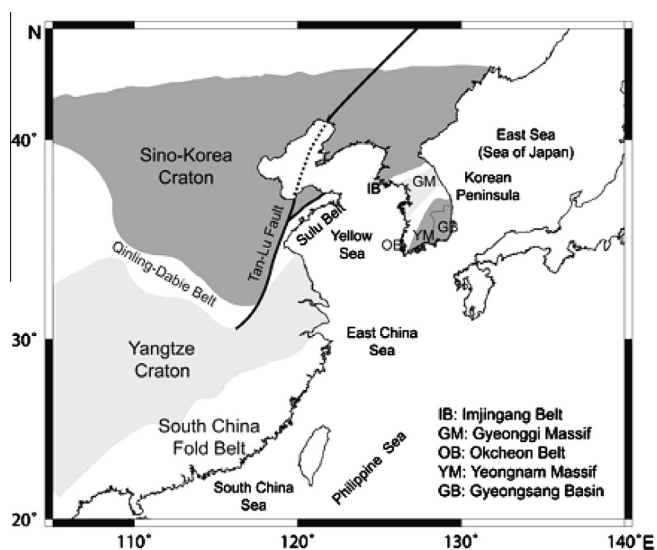


Fig. 1. Simplified tectonic map of East Asia. Folded belt areas are illustrated in white, and cratons and massifs are depicted in gray. Faults are represented by thick solid lines (from Chang and Baag, 2007).

high-frequency bands. Synthetic Green functions (SGF) and empirical Green functions (EGF) are adopted for the low-frequency and the high-frequency bands, respectively. A grid search method is applied to four parameters: the strike, dip, rake, and focal depth of rupture nucleation. For each set of grid-searched parameters, the spatial and temporal slip distribution was recovered on the two nodal planes of the focal mechanism using a least squares waveform inversion technique. We compare the obtained results in both low- and high-frequency bands. The results contribute to the tectonic implication of the eastern part of the Gyeonggi Massif (Fig. 1).

2. Tectonic settings

The SKP is located in the northeastern Asia margin, a convergent region of the China continent and the Japanese Island Arc. This arc is characterized by the subduction of the Philippine Sea plate and the southeastward expulsion of the Eurasian plate (Molnar and Tapponnier, 1975; Zonenshain and Savostin, 1981; Kato et al., 1998; Kogan et al., 2000; Jin and Zhu, 2003; Jin and Park, 2006; Jin et al., 2007). The focal mechanisms for intraplate earthquakes in the SKP show predominant strike-slip faults with minor reverse or normal components (June, 1990; Kim, 1993; Kim et al., 2004; Park et al., 2007).

The geology of the SKP mainly consists of four tectonic provinces: running from northwest to southeast, the Imjingang belt, the Gyeonggi massif, the Okcheon belt, and the Yeongnam massif (Fig. 1). The Imjingang belt is an east-west-trending fold and thrust zone consisting of metasedimentary rocks and volcanoclastics (Devonian–Carboniferous), underlain unconformably by Proterozoic basement rocks (Chough et al., 2000). Two Precambrian metamorphic massifs, the Gyeonggi and the Yeongnam massifs, separated by the Phanerozoic Okcheon belt, which consists of high-grade schists and gneisses (Sagong et al., 2005). A Cretaceous sedimentary basin named the Gyeongsang basin lies on the southeastern part of the Yeongnam massif.

The epicenter of the Odaesan earthquake is located in the eastern part of the Gyeonggi Massif. The geology of the source region is composed mainly of Jurassic granite, porphyroblastic gneiss, migmatitic gneiss, and Cretaceous sedimentary rocks. The area has been intruded by Jurassic granite and is partly blanketed with Cretaceous sediments. Two dominant fault trends are known in the epicentral area. The first is the Woljeongsa fault that runs N10°E

along a small river, Odacheon, at distance of 1 km to the east of the epicenter in the area of Jurassic granite (Jo and Baag, 2007). The second is the South Korean Tectonic Line (SKTL) and represents the major tectonic boundary between the Gyeonggi Massif and the Yeongnam Massif (Chough et al., 2000).

3. Data analysis

3.1. Data used

Waveform data used in the present study were recorded by the digital seismographic networks operated by the Korean Meteorological Administration (KMA). The January 2007 Odaesan earthquake sequence started on 17 January 2007 at 16:03:02, which was followed by over 45 microearthquakes as observed by Kim et al. (2010) through scanning continuous waveform data recorded at the nearest station DGY. Only nine foreshocks and nine aftershocks were locatable by Kim et al. (2010) with coda-duration magnitudes (M_D) larger than 1.0 based on the formula given by Tsumura (1967). The Odaesan earthquake triggered almost all broadband and short-period stations in the SKP, as well as a dense network of accelerometers. Based on the double-couple point source assumption, two fault-plane solutions have been reported for the Odaesan earthquake: one solution (strike = 20°, dip = 70°, rake = −165°) was retrieved from the polarities of P_g , P_n and SH waves (Jo and Baag, 2007), and the other solution (strike = 115°, dip = 85°, rake = −5°) was determined from the waveform modeling done by Herrmann (2007). The solution (strike = 115°, dip = 88°, rake = −6°) was obtained by Kim (2007) from the moment tensor inversion.

To investigate the finite source model of the Odaesan earthquake in both low- and high-frequency bands, we used the waveform data recorded by the stations within an epicentral distance of less than 70 km. The selected stations consisted of two broadband stations, three short-period stations and two force-balance accelerometers (ES-T). The sampling intervals of these instruments are all 100 samples per second. The earthquake locations used in the present study and the seismic stations are shown in Fig. 2. The spatial distribution of stations around the epicenter is satisfactory and helps in better constraining the solution.

The focal mechanisms of the foreshocks and aftershocks were determined using the amplitude spectra and P -wave polarities. A computer program developed by Zahradnik et al. (2001) was used to determine the fault plane solutions. The focal and fault plane parameters of the mainshock, foreshocks, and aftershocks are listed in Table 1. For the mainshock analysis, the waveform data were analyzed in low- and high-frequency bands. The waveform data were filtered with frequency bands of 0.1–0.3 and 1.0–3.0 Hz for the low- and high-frequency bands, respectively. A linear trend was removed and the data were corrected to ground velocity. The velocity model used in the present study to calculate synthetic Green functions is listed in Table 2.

3.2. Analysis of foreshocks and aftershocks

To use a small event as an empirical Green function (EGF), its magnitude should be small enough to be considered as a delta function in space and time, and large enough to be recorded with good signal-to-noise ratios at all the relevant stations. In addition, both the large and small events should have similar focal mechanisms and hypocenters. We relocated the hypocenters using P - and S -wave arrival times and the iterative technique based on Geiger's method. The epicenters of relocated events cluster around the mainshock location (Fig. 2).

Focal mechanisms of the available foreshocks and aftershocks were calculated using a recently developed method by Zahradnik

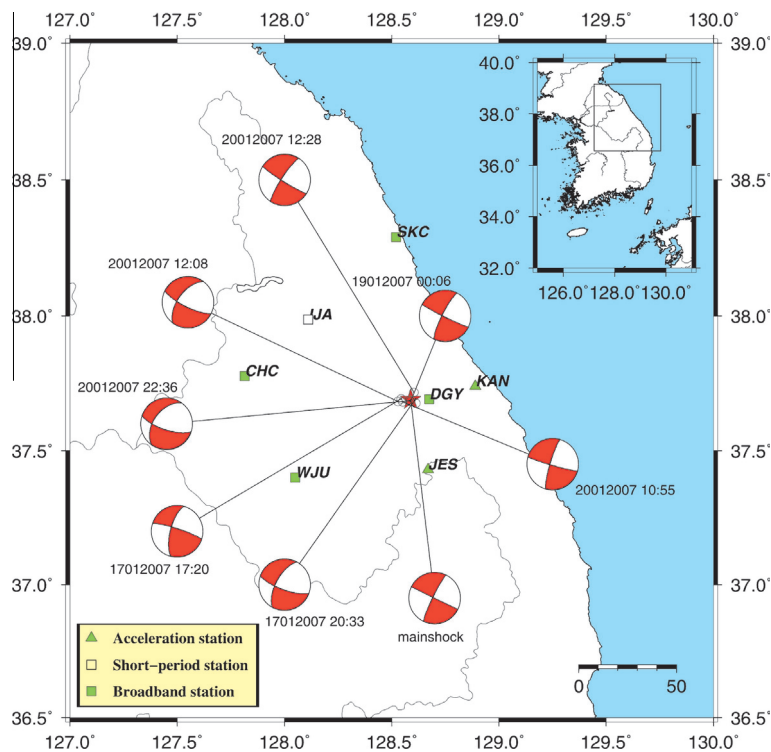


Fig. 2. Map showing locations of the Odaesan earthquake (solid star) and its foreshocks and aftershocks (open circles) and KMA stations. The focal mechanisms of the mainshocks and the foreshocks and aftershocks events are also shown. These indicate almost strike-slip fault motions with normal components.

et al. (2001) and Zahradnik (2002). This method is based on the amplitude spectra of complete three-component waveform data and the first-motion polarities, hereafter ASPO. The waveforms recorded by velocity sensors at nearest local stations were employed. The take-off angles were calculated using the ray-method code ANGGRA (Jansky, 2001). In the ASPO method, the amplitude spectra were analyzed using complete three-component velocity waveforms of 60 s duration in the frequency range 1.0–2.0 Hz. The spectra were then modeled by the discrete wave-number method of Bouchon (1981) and Coutant (1989), using the velocity model listed in Table 2. A grid-search method was applied to three parameters: strike, dip, and rake angles. For each set of these model parameters, both the observed and synthetic spectra were normalized in order to put them on a comparable amplitude level. The normalization was performed by dividing the spectra by their average value computed for all components and frequencies at all available stations (taken over all stations, components and frequencies). The misfit at each station was calculated as a weighted

Table 2
Velocity structure used to calculate Green's functions and locate foreshocks and aftershocks.

Depth (km)	P-vel. (km/s)	S-vel. (km/s)	Depth (g/cm ³)
0.0	4.49	2.56	2.60
1.1	5.46	3.12	2.79
2.1	5.72	3.27	2.84
3.1	5.95	3.40	2.89
10.6	6.36	3.63	2.97
18.6	6.63	3.79	3.03
24.6	7.04	4.02	3.11
26.6	7.22	4.12	3.14
28.6	7.53	4.30	3.21
30.6	7.62	4.35	3.22
32.6	7.98	4.56	3.30

L1 norm of the difference between the observed and synthetic amplitude spectra, and then summed up over all stations, components and frequencies. The misfit function introduced in Zahradnik

Table 1
Hypocentral and fault plane parameters of the events considered in the present study.

ID	Date	O.T.	Lat.	Long.	Depth	Mw	Plane I			Plane II			Ref
							ϕ	δ	λ	ϕ	δ	λ	
–	20070117	17:20:10.40	37.7162	128.6034	12	2.3	288	88	22	197	68	178	*
–	20070117	20:33:51.38	37.6823	128.5875	12	2.4	110	74	–28	208	63	–162	*
EV1	20070119	00:06:23.75	37.6765	128.6127	12	2.8	116	86	–10	20	70	–165	*
EV2	20070120	10:55:21.19	37.6817	128.5514	12	2.6	106	84	–08	197	82	–174	*
Main	20070120	11:56:53.48	37.6860	128.5890	12	4.5	284	76	–21	205	85	–175	JB
		11:56:53.53	37.6870	128.5840	9	4.6	115	85	–05	204	88	–180	HR
					10	4.7	116	90	–06	206	84	–180	*
–	20070120	12:28:03.02	37.6852	128.5835	14	2.6	216	58	–162	116	75	–033	*
EV3	20070117	22:36:03.21	37.6826	128.5285	12	2.7	122	84	–10	213	80	–174	*
–	20070117	17:20:10.40	37.7162	128.6034	14	2.5	216	49	–154	108	71	–044	*

ϕ : strike, δ : dip, λ : rake, JR: Jo and Baag (2007), HR: Herrmann(2007).
* This study.

et al. (2001) not only reduces undesired biasing effect of the largest amplitude at the near stations, but also normalizes the misfit values between 0 and 1. Here, amplitude spectra solutions were constrained with first-motion polarities to obtain optimum solutions whose misfits are between $\pm 5\%$. The procedure was repeated for a set of ten trial source depths. We started with a coarse search with a broad depth range (5–50 km), and then a fine search was focused around the minimum misfit value in a narrow depth range (4–20 km). Finally, the scalar moment was retrieved with no grid-search procedure since the problem is linear with respect to the scalar moment. Instead of grid searching, unit-moment synthetic spectra were calculated for the preferred mechanism and depth, and the ratio (averaged over all data) between the observed and synthetic spectra then yields the moment (Zahradnik et al., 2004).

For this analysis, we used amplitudes of complete seismograms after band-pass filtering from 1.0 to 2.0 Hz. To find the best-fit double-couple solution, the strike, dip, and rake were finely searched at 2° intervals. Table 1 shows the hypocenter and two nodal planes of the focal mechanism for each event. The focal mechanism solutions are shown in Fig. 2. Fig. 3a shows an example of the variation of the amplitude-spectra misfit with trial focal depths. It also shows the corresponding focal mechanisms determined using the amplitude spectra constrained by first-motion polarities for the event occurring on 20 January 2007 at 12 h 28 m. Fig. 3b shows the best-fit double-couple solution consistent with P-wave polarities. The analyzed events show strike-slip faulting mechanisms with a normal component compatible with the stress field in the Korean peninsula.

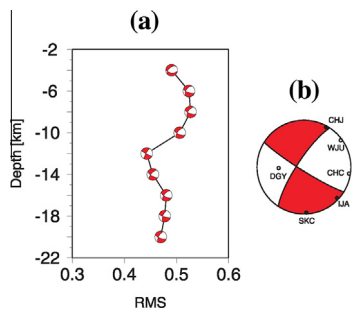


Fig. 3. Fault plane solution of the event 20/01/2007 12 h:28 m. (a) Optimal best double-couple orientations for a range of source depth. (b) The optimal best double-couple focal mechanism constrained with P-wave polarities at focal depth 12 km.

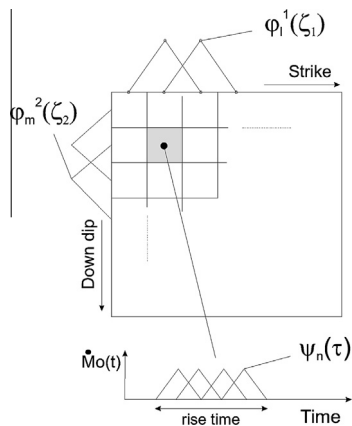


Fig. 4. Illustration of knot distribution and isosceles multi-time windows. The source is expressed as an expansion of isosceles time windows $\psi_n(\tau)$ and spatial windows $\varphi_1^1(\zeta_1)$ and $\varphi_m^2(\zeta_2)$. Each window corresponds to an unknown source parameter (Eq. (2)).

3.3. Finite-source model

The waveform modeling method provides a rupture process for an earthquake as a sequence of double-couple point sources. These point sources are generally assumed to have the same fault plane. In this study, a grid-search method is applied over four parameters: strike, dip, rake, and focal depth of the nucleation rupture. For each set of grid-search parameters, the spatiotemporal slip distribution on the fault plane (strike and dip) was recovered using waveform inversion. The spatiotemporal slip distribution was expanded by Ide and Takeo (1997) for a specific i^{th} component of focal mechanisms on the lm subfault as:

$$\Delta u_i(\zeta_1, \zeta_2, \tau) = \sum a_{ilmn} \varphi_1^1(\zeta_1) \varphi_m^2(\zeta_2) \psi_n(\tau) \quad (1)$$

where $\zeta = (\zeta_1, \zeta_2)$, a_{ilmn} are expansion coefficients and $\varphi_1^1(\zeta_1)$, $\varphi_m^2(\zeta_2)$, and $\psi_n(\tau)$ are the basis functions in strike, dip and time axes, respectively. Each basis function is an isosceles triangle determined by three knots, and hence the slip is spatially and temporally continuous everywhere. The spatiotemporal slip distributions are defined by basis functions arranged on the assumed fault plane and the time axis. To expand the spatiotemporal distribution of the displacement over the assumed fault using the basis functions, the knots of the isosceles triangles are arranged into a 3D spatiotemporal space, a 2D fault plane (strike & dip) and the time axis. Fig. 4 shows the schematics of a fault plane and the source time functions used in the inversion. The observed seismogram from a finite-fault model is given as:

$$U_j^{\text{obs}}(x, t) = \sum_{+e_j(x,t)} a_{ilmn} \iiint M_{i,k}(\zeta, \tau) g_{ji,k}(x, t, \zeta, \tau) \varphi_1^1(\zeta_1) \varphi_m^2(\zeta_2) \psi_n(\tau) d\zeta_1 d\zeta_2 d\tau \quad (2)$$

where $M_{ik}(\zeta, \tau)$ and $g_{ji,k}(x, t, \zeta, \tau)$ are the seismic moment tensor component and the Green function at the point ζ on the lm subfault, and $e_j(x, t)$ is the error function between the observed and synthetic seismograms. M_{ik} are related to the orientation of the fault and auxiliary planes for double-couple point sources. They are as follows (Aki and Richards, 1980):

$$\begin{aligned} M_{11} &= \sin \delta \cdot \cos \lambda \cdot \sin 2\varphi - \sin 2\delta \cdot \sin \lambda \cdot \sin^2 \varphi \\ M_{12} = M_{21} &= \sin \delta \cdot \cos \lambda \cdot \cos 2\varphi + \frac{1}{2} \sin 2\delta \cdot \sin \lambda \cdot \sin 2\varphi \\ M_{13} = M_{31} &= \cos \delta \cdot \cos \lambda \cdot \cos \varphi + \cos 2\delta \cdot \sin \lambda \cdot \sin \varphi \\ M_{22} &= \sin \delta \cdot \cos \lambda \cdot \sin 2\varphi - \sin 2\delta \cdot \sin \lambda \cdot \cos^2 \varphi \\ M_{23} = M_{32} &= -\cos \delta \cdot \cos \lambda \cdot \sin \varphi + \cos 2\delta \cdot \sin \lambda \cdot \cos \varphi \\ M_{33} &= 0 \end{aligned} \quad (3)$$

where φ , δ and λ are the strike, dip and rake of the fault planes. The observational equation can be written in a vector form as:

$$d = Gm + e \quad (4)$$

where d is the vector composed of the observed waveform for the large event, m is the model parameter vector of a_{ilmn} , e is assumed to be the Gaussian error with a mean of zero and a variance of σ , and the $(N \times M)$ G represents the synthetic waveform data expanded by the triangle basis functions. The matrix terms N and M are the number of data points at the recorded stations and the number of model parameters, respectively. We have found, in general, that an increase in the number of model parameters leads to a decrease in error and an increase in the instability of the solution. This provides an initial result where any slight change in the data may create a large change in the solution. To obtain more stable results, we applied smoothing constraints to the slip distribution with respect to the space (D_s) and the time (D_t) by following Ide et al. (1996). Hence, the observational Eq. (4) can be rewritten as:

$$\begin{bmatrix} G \\ \alpha_1 D_s \\ \alpha_2 D_t \end{bmatrix} = \begin{bmatrix} d + e \\ e_1 \\ e_2 \end{bmatrix} \quad (5)$$

where $\alpha_1 = \sigma/\sigma_1$ and $\alpha_2 = \sigma/\sigma_2$ are hyper-parameters that represent the relative weights of the corresponding constraints, e_1 and e_2 are Gaussian errors with means of zero and covariance of $\sigma_1^2 I$ and $\sigma_2^2 I$, and I is an identity matrix. The factors α_1, α_2 are determined by Akaike's Bayesian information criterion (ABIC), which is formulated on the principle of maximizing entropy and defined as minus twice the marginal likelihood (Akaike, 1980). Refer to Ide et al. (1996) for details. Eq. (5) was solved using the non-negative least-squares (NNLS) inversion technique (Lawson and Hanson, 1974) to constrain the slip distribution on the fault plane.

4. Results and discussions

The identification of the actual fault plane with a finite fault model over a wide range of earthquake magnitudes has already been considered using different methods and data sets. Actual fault planes have been determined using additional information such as surface rupture, aftershock distribution (Örgülü and Aktar, 2001; Badawy and Abdel-Fattah, 2002; Ozalaybey et al., 2002; Chen et al., 2003), nearby active tectonic structures, rupture process

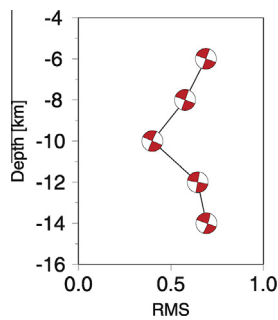


Fig. 5. Variation of the RMS error between the observed and synthetic seismograms over strike, dip and rake with five trial focal depths using a finite-source model.

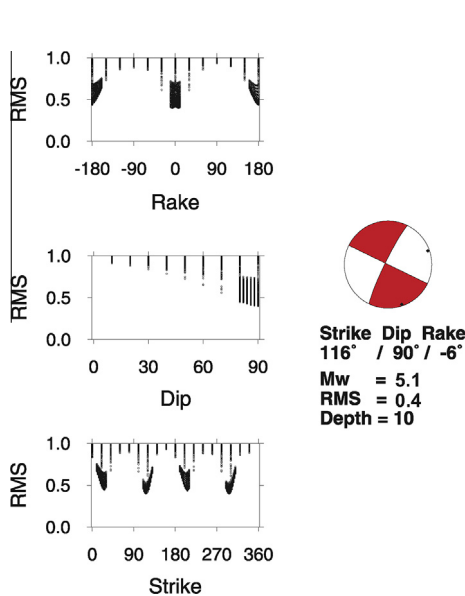


Fig. 6. Results of waveform inversion with a grid search over strike, dip, and rake in the low-frequency band. Four triplets with the lowest RMS are observed along the WNW and NNE directions. The WNW-striking trend gives the smallest RMS error.

inversion (Hartzell and Heaton, 1986; Mori and Hartzell, 1990; Abercrombie et al., 2001; Delouis et al., 2002), rupture directivity (Mori and Hartzell, 1990; Velasco et al., 1994; Li et al., 1995; Abdel-Fattah and Badawy, 2002), and stopping phases (Imanishi et al., 2004). In the present study, the finite-source model for the Odaesan earthquake was investigated using the bandpass-filtered seismograms in both low- and high-frequency bands.

The technique described in the low-frequency band is similar to that of one introduced by Legrand and Delouis (1999) and Delouis and Legrand (1999), but the slip is expanded in space and time by basis functions with unknown expansion coefficients (Ide and Takeo, 1997). No prior information is required for rupture dimensions. Using the filtered seismograms in the low-frequency band, the grid search over the strike, dip, rake, and focal depth was performed to find the best-fit double-couple mechanism and the hypocenter of rupture nucleation. The selection criterion in the grid search was the minimization of the normalized root mean squares (RMS) error between the observed and synthetic seismograms. The procedure was repeated at a few trial source depths

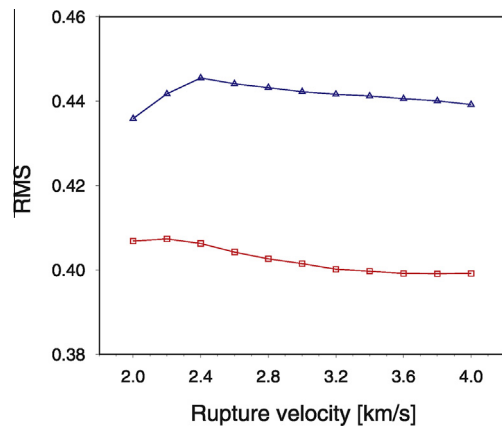


Fig. 7. Variations of RMS error for a set of low-frequency rupture models recovered on the two nodal planes with various rupture velocities in the range of 2.0–4.0 km/s; the NW (squares) and the NNE (triangles).

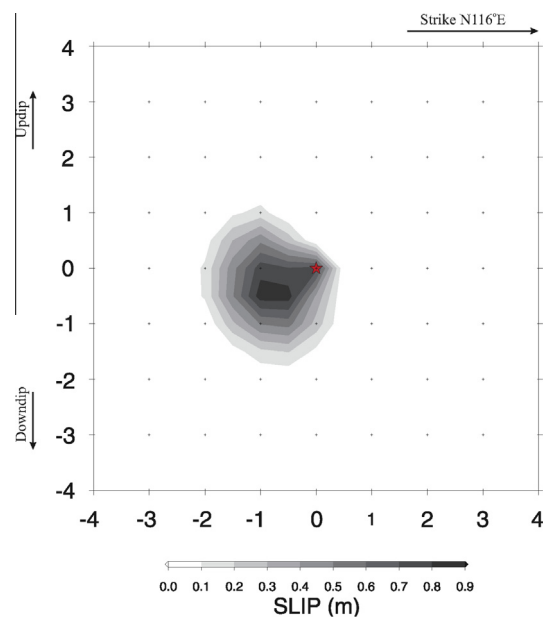


Fig. 8. Low-frequency slip model as inferred from a non-negative least-square inversion along the WNW-striking trend.

in a coarse search followed by a fine search around the minima of the RMS misfit function. The spatiotemporal slip distribution was recovered for each set of the grid-search parameters. We carried out the waveform inversion using a fault area of 4×4 km to retrieve the rupture process. We used node intervals of 0.5 km along both the strike and the dip axes. Along the time axis, the slip-rate function on each subfault was expanded into a series of nine triangle functions with rise times of 1.0 s. For all the grid-search trials that are shown in Fig. 5, the focal depth of rupture nucleation was determined to be 10 km and the best-fit double-couple solution exhibited two possible vertical strike-slip mechanisms. The four triplets that give the smallest RMS errors (Fig. 6) correspond to four nodal planes running along the NNE and WNW trends with a change of $\pm 180^\circ$ in both strike and rake. Two solutions are solved to be (strike, dip, rake) = $(116^\circ, 90^\circ, -6^\circ)$ and $(296^\circ, 90^\circ, 6^\circ)$ with the corresponding auxiliary plane $(206^\circ, 84^\circ, 180^\circ)$ and $(206^\circ, 84^\circ, -180^\circ)$. It is obvious from Fig. 6 that the lower RMS values, for each discrete value of the strike, dip and rake parameters, dis-

played much finer sampling corresponded to the region of the best solutions obtained from fine grid search around the minima of the RMS resulting from the coarse search. The WNW-striking plane gives a better fit than the conjugate NNE-striking plane. The variance reduction was increased by 5%. To verify the actual fault plane in the low-frequency analysis, the two planes (WNW and NNE) were tested with various rupture velocities. The range of rupture velocity is 2.0–4.0 km/s. The values of RMS errors with a varying rupture velocity are shown in Fig. 7. For all rupture velocities, the WNW-striking trend gives a smaller RMS than the NNE-striking trend. Fig. 8 shows the slip distribution in the WNW-striking trend with a rupture velocity of 3.2 km/s. The comparison between the observed and synthetic waveforms inverted from the slip distribution model (Fig. 8) shows that the fit is satisfactory which proves that the velocity model (Table 2) is adequate for frequencies lower than 0.3 Hz (Fig. 9). To consider such information in higher frequencies, we extended the frequency band from 0.1–0.3 Hz to 0.1–0.5 Hz in the waveform inversion. The variance reduction decreased by 10%, reflecting that the available velocity model in the respective region is not represented enough to calculate synthetic Green functions higher than 0.5 Hz.

It is typically not possible to calculate an appropriate synthetic waveform for the Odaesan earthquake in the high-frequency band, because we must know the velocity structure of the earth in a scale of a few kilometers, which is seldom achievable. Therefore, we use the EGF (e.g. Hartzell, 1978; Mueller, 1985; Frankel et al., 1986) to recover the slip distribution. Finite source characteristics for small- to moderate-sized earthquakes are derived using empirical Green functions (EGF) that are often employed to account for propagation path effects (Mori, 1996; Hellweg and Boatwright, 1999; Okada et al., 2001; Okada et al., 2003; McGuire, 2004). The multiple time-window method described in the present study has been applied for small-, moderate- and large-sized earthquakes (Ide and Takeo, 1997; Ide, 2000; Okada et al., 2001; Abdel-Fattah, 2002; Abdel-Fattah et al., 2011). The method has also been applied to small-sized earthquakes induced in a South African gold mine (Yamada et al., 2005).

Source inversions using an EGF are strongly affected by the selection of the EGF event. The present source process inversion was performed using three different EGF events, with moment magnitudes of 2.6, 2.7, and 2.8. Slip distributions for each inversion are shown in Fig. 10. The slip distribution maps are almost identical to each other. The comparison between observed and synthetic waveforms for high-frequency rupture models is shown in Fig. 11. We used the same stations as in the low-frequency analysis to compare the results in both frequency bands. We carried out the waveform inversion using a fault area of 4×4 km to retrieve the rupture process. We used node intervals of 0.5 km along both the strike and the dip axes. Along the time axis, the slip-rate

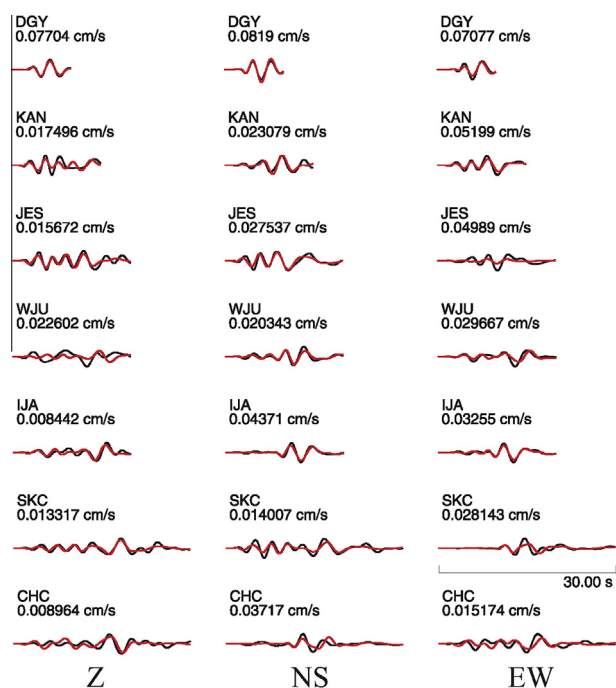


Fig. 9. Comparison between observed (black lines) and synthetic (red lines) waveforms obtained from the rupture model with rupture velocities of 3.2 km/s. Station code and maximum amplitude in cm/s are indicated in the upper left corner of each set of traces, respectively. (For interpretation of the references to colour in this figure legend, the reader is referred to the web version of this article.)

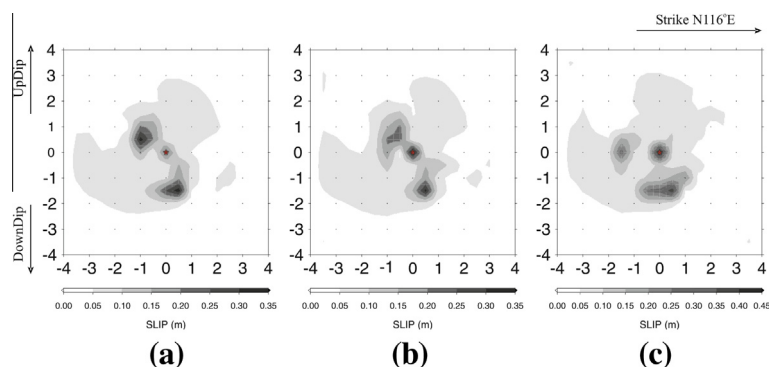


Fig. 10. Total slip models recovered on the NNE-striking trend using the records of three empirical Green's functions: (a) EV1, (b) EV2, and (c) EV3, respectively.



Fig. 11. Comparison between observed (black lines) and synthetic (red lines) waveforms obtained from the rupture model with rupture velocities of 3.2 km/s using the records of three empirical Green's function: (a) EV1, (b) EV2, and (3) EV3. Station code and maximum amplitude in counts are indicated in the upper left corner of each set of traces, respectively. (For interpretation of the references to colour in this figure legend, the reader is referred to the web version of this article.)

function on each subfault was expanded into a series of nine triangle functions with rise times of 1.0 s.

The nodal planes (strike = 116° and 206° and dip = 90° and 84°) of the mainshock focal mechanisms were tested with various rupture velocities. The range of rupture velocity is 2.0–4.0 km/s. Fig. 12 shows the RMS errors between calculations and

observations in the three inversions at changing rupture velocity. The smallest RMS was obtained in the case of EGF 19 January 2007 00 h 06 m *M* 2.8, the largest foreshock. For all rupture velocities, the SW dipping plane gives smaller RMS errors than its conjugate plane. From the aforementioned results exhibited that the NW plane were slipped and emitted seismic waves with different

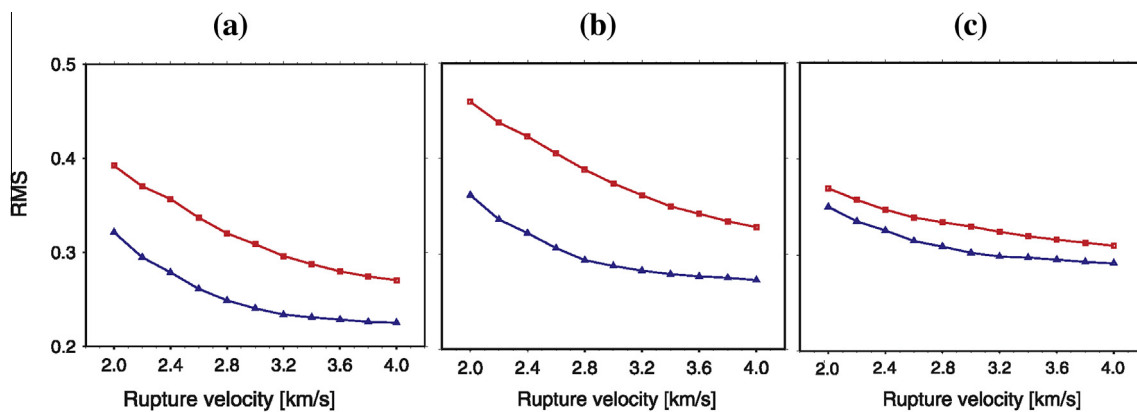


Fig. 12. RMS error of the waveform for different rupture velocities in the range of 2.0–4.0 km/s on the two nodal planes; the NW (triangles) and the NE (squares) using the records of three empirical Green's functions: (a) EV1, (b) EV2, and (c) EV3, respectively.

frequency contents. The recovered slip models on both nodal planes (Fig. 10) exhibited oblique patterns of asperities around the hypocenter. The spectrogram of the *P*-wave records at JES station showed complex patches in different frequency bands (Fig. 13). Tectonically, if we preferred the westward-dipping plane as the actual fault plane, this implies that the slip was a dextral strike-slip on the NNE-trending plane dipping toward the west. This trend is tectonically conjugated to the Wolgosaen fault that runs N10°E in the epicentral area. This trend is consistent with the eastern edge of the basin imaged in the epicentral area by the Moho depth variations estimated from receiver functions (Yoo et al., 2007). However, the fault plane may not be related to that of suggested nearby mapped structures, particularly if the earthquake source is caused by a blind fault at depth or an unmapped subsidiary faults at the surface. Our investigations in the low- and high-frequency bands indicate sinistral strike-slip faulting along the NW striking trend that is tectonically represented the conjugate plane in the respective area which in consistency with the double-difference relocations by Kim et al. (2010) and Kim and Park (2010). Moreover, the most likely quaternary faults that generate earthquakes in the SKP run along the NNE- to NNW-striking faults with a high-angle dextral strike-slip or/and an oblique-slip with a reverse component (Park et al., 2007). The sinistral strike-slip movement along the NW direction in the SKP

was shown in the neotectonic fault map presented by Kim et al. (2004). Whatever the actual fault plane of the Odaesan earthquake is, the obtained focal mechanism shows an ENE–WSW compression stress axis and a NNW–SSE extension stress axis coinciding with the principle horizontal axes of extension and compression derived by Jin and Park (2007). These were derived from the analysis of strain rates using continuous GPS observations (2000–2004) and fault plane solutions for recent earthquakes with an $M_w \geq 4$ in and around the SKP from 1936 to 2004. This stress pattern is consistent with the tectonic stress orientation in neighboring north-eastern China and southwestern Japan, which is attributed to the relative motion between the tectonic plates in the region. Based on the mangerite compositions in the Odaesan epicentral area, Oh et al. (2006) supposed that the tectonic belt connecting the Hongseong and Odaesan areas represents a probable extension of the late Permian–Triassic collision between the North and South China blocks into SKP, with collision occurred earlier in the SKP.

A smooth rupture model was recovered in the low-frequency analysis as shown in Fig. 8, the so-called coherent rupture model. The rupture of one distinct asperity was initiated with a relatively low amount of slip and was propagated smoothly westwards from the hypocenter. Fig. 10a–c show the slip distribution models recovered in the high-frequency analysis; three rupture histories correspond to the models using EV1, EV2, and EV3, respectively. The

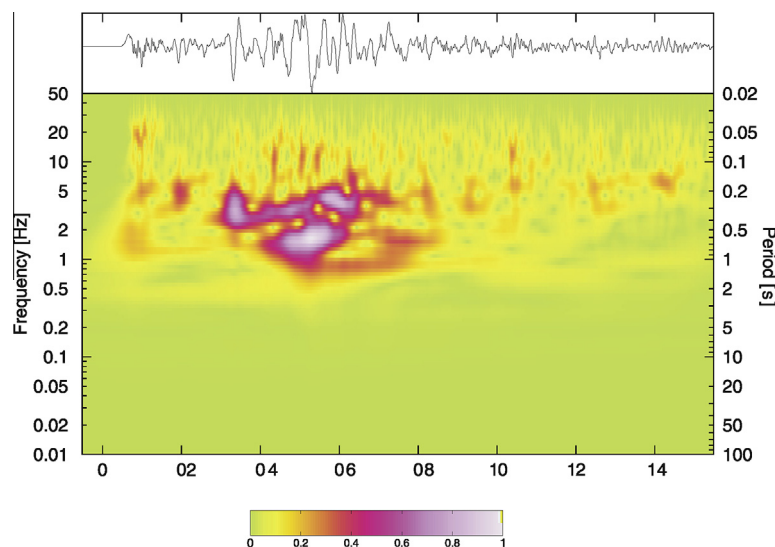


Fig. 13. The spectrogram for *P*-wave records at the JES station 30 km away from the epicenter of Odaesan earthquake.

rupture initiates with a relative large amount of slip and two small asperities have been obliquely observed down and upwards from the hypocenter to the SE and NW trends, respectively. This slip distribution pattern is in consistence with the results obtained by Park and Hahm (2010). The overall patterns of the three models are almost identical and exhibit complex rupture behaviors, the so-called incoherent rupture models, which consistent with the complex relative source time functions retrieved by Kim et al. (2010). The incoherent rupture models radiated high-frequency waves due to the breakage of small asperities or patches throughout the fault plane (Papageorgiou and Aki, 1983; Koyama, 1985). In these models, many small-scaled asperities or patches are expected to be distributed randomly throughout the fault plane. The relationship between the location of high-frequency wave radiation and low-frequency wave radiation may be controlled by the heterogeneous distribution of stress and/or strength on the earthquake fault (Nakahara et al., 2002).

The low- and high-frequency rupture models give seismic moments of 7.7×10^{16} Nm and 8.0×10^{16} Nm, respectively. In the high-frequency analysis, the amplitude of slip is estimated using the seismic moment of small events and the moment ratio between the mainshock and small events. Accordingly, the high-frequency analysis experiences uncertainty due to an error in estimating the seismic moment of small events. Moreover, the discrepancy between the seismic moments determined from the low- and high-frequency analysis may attribute to the dissimilarity between the seismic radiations in both frequency bands. The seismic moments obtained from finite-source models are higher than those obtained from other studies assuming point-source models (e.g. Jo and Baag, 2007), suggesting that some dislocations took place from the region surrounding the asperities patches in the finite-source models.

5. Conclusions

A set of finite fault models for the Odaesan earthquake in both low- and high-frequency bands was constructed. Synthetic Green functions and empirical Green functions (EGF) were adopted for the low-frequency band and high-frequency band, respectively. In the low-frequency analysis, a simple rupture propagation behavior was represented, while a complex behavior was observed in the high-frequency one. The fault plane solution obtained from the finite-fault model in the low- and high frequency bands indicates a vertical strike-slip faulting mechanism with sinistral movement along the NW striking trend. In both frequency bands the difference in variance reduction, produced by the actual fault plane and its auxiliary, is about 5%. Neotectonic studies in the SKP have shown that the most likely quaternary faults that generate earthquakes in the region are running along the NE- to NW-striking faults. For high-frequency band, the main finding in the present study indicates a complex rupture history for such moderate-sized earthquakes that is similar to those reported for large-sized earthquakes. It seems that the scenario of the complex rupture history obtained in the present study does not depend on earthquake size; giving self-similar behavior likes that reported for large-sized earthquakes.

Acknowledgments

This work was funded by the Brain Pool Program under the Grant 072-1-3-0262. The authors acknowledge the assistance of the many people at the KMA who participated in preliminary data analyses. The work was revised at the Geology and Geophysics Dept., Collage of Science, King Saud University. At the revision stage, the work was supported by King Saud University, Deanship

of Scientific Research, College of Science Research Centre. Slip distribution models were computed using the STINV package developed by Satoshi Ide, Department of Earth and Planetary Science, Univ. of Tokyo, Japan. For finite source model, the synthetic Green's functions were calculated using the computer programs in seismology developed by R. Herrmann, S. Louis Univ., USA. Comments by the editor and two anonymous reviewers were very helpful in improving the paper.

References

- Abdel-Fattah, A.K., 2002. Source characteristics of a moderate earthquake (M 4.9) using the empirical Green's function technique. *Ann. Geophys.* 45 (5), 575–586.
- Abdel-Fattah, A.K., Badawy, A., 2002. Source process of the southeast Beni-Suef, northern Egypt earthquake using empirical Green's function technique. *J. Seismolog.* 6 (2), 153–161.
- Abdel-Fattah, A.K., Kim, K.Y., Fnaï, M.S., 2011. Slip distribution model of two small-sized inland earthquakes and its tectonic implication in north-eastern desert of Egypt. *J. Afr. Earth Sci.* 61 (4), 296–307.
- Abercrombie, R.E., Bannister, S., Pancha, A., Webb, T., Mori, J., 2001. Determination of fault planes in a complex aftershock sequence using two-dimensional slip inversion. *Geophys. J. Int.* 146, 134–142.
- Akaike, H., 1980. Likelihood and Bayes procedure. In: Bernardo, J.M. et al. (Eds.), *Bayesian Statistics*. University Press, Valencia, Spain, pp. 143–166.
- Aki, K., Richards, P., 1980. *Quantitative Seismology: Theory and Methods*. W.H. Freeman, New York.
- Badawy, A., Abdel-Fattah, A.K., 2002. Analysis of the southeast Beni-Suef, northern Egypt earthquake sequence. *J. Geodyn.* 33, 219–234.
- Bouchon, M., 1981. A simple method to calculate Green's functions for elastic layered media. *Bull. Seismol. Soc. Am.* 71, 959–971.
- Chang, S.-J., Baag, C.-E., 2007. Moho depth and crustal V_P/V_S variation in Southern Korea from teleseismic receiver functions: implication for tectonic affinity between the Korean Peninsula and China. *Bull. Seismol. Soc. Am.* 97, 1621–1631.
- Chen, C.-H., Wang, W.-H., Teng, T.-L., 2003. A possible causal relationship between the 1998 Ruyi-Li sequence and the 1999 Chi-Chi earthquake in Taiwan. *Bull. Seismol. Soc. Am.* 93, 1542–1558.
- Chough, S.K., Kwon, S.-T., Ree, J.-H., Choi, D.K., 2000. Tectonic and sedimentary evolution of the Korean peninsula: a review and new view. *Earth Sci. Rev.* 52, 175–235.
- Coutant, O., 1989. Program of Numerical Simulation AXITRA. Research Report, LGIT, Grenoble.
- Delouis, B., Giardini, D., Lundgren, P., Salichon, J., 2002. Joint inversion of InSAR, GPS, teleseismic, and strong motion data for the spatial and temporal distribution of earthquake slip: application to the 1999 Izmit mainshock. *Bull. Seismol. Soc. Am.* 92, 278–299.
- Delouis, B., Legrand, D., 1999. Focal mechanism and identification of the fault plane of earthquakes using only one or two near source seismic recordings. *Bull. Seismol. Soc. Am.* 89, 1558–1574.
- Frankel, A., Fletcher, J., Vernon, F., Haar, L., Berge, J., Hanks, T., Brune, J., 1986. Rupture characteristics and tomographic imaging of $M_L = 3$ earthquakes near Azna southern California. *J. Geophys. Res.* 91, 12633–12650.
- Hartzell, S.H., 1978. Earthquake aftershocks as Green's functions. *Geophys. Res. Lett.* 5, 1–4.
- Hartzell, S.H., Heaton, T.H., 1986. Rupture history of the 1984 Morgan Hill, California earthquake from the inversion of strong motion records. *Bull. Seismol. Soc. Am.* 76, 649–674.
- Hellweg, M., Boatwright, J., 1999. Mapping the rupture process of moderate earthquakes by inverting accelerograms. *J. Geophys. Res.* 104, 7319–7328.
- Herrmann, R. B., 2007. Available from: <http://mnw.eas.slu.edu/Earthquake_Center/MECH.KR>.
- Ide, S., 2000. Complex source processes and the interaction of moderate earthquakes during the earthquake swarm in the Hida-Mountains, Japan, 1998. *Tectonophysics* 334, 35–54.
- Ide, S., Takeo, M., 1997. Determination of constitutive relations of fault slip based on seismic wave analysis. *J. Geophys. Res.* 102, 27379–27391.
- Ide, S., Takeo, M., Yoshida, Y., 1996. Source process of the 1995 Kobe earthquake: determination of spatio-temporal slip distribution by Bayesian modeling. *Bull. Seismol. Soc. Am.* 86, 547–566.
- Imanishi, K., Takeo, M., Ellsworth, W.L., Ito, H., Matsuzawa, T., Kuwahara, Y., Iio, Y., Horiuchi, S., Ohmi, S., 2004. Source parameters and rupture velocities of microearthquakes in western Nagano, Japan, determined using stopping phases. *Bull. Seismol. Soc. Am.* 94, 1762–1780.
- Jansky, J., 2001. Ray-method Calculations of the Travel Times and Take-off Angles in Gradient Models, Program ANGGRA, Research Report, Dept. of Geophysics, Faculty of Math. and Phys., Charles University, Prague.
- Jin, S., Park, P.H., 2006. Strain accumulation in South Korea inferred from GPS measurements. *EPS* 85, 529–534.
- Jin, S., Park, P.H., 2007. Tectonic activities and deformation in South Korea constrained by GPS observations. *Int. J. Geol.* 1, 11–15.
- Jin, S.G., Zhu, W.Y., 2003. Active motion of tectonic blocks in eastern Asia: evidence fro GPS measurements. *ACTA Geol. Sin. (English ed.)* 77 (1), 59–63.

- Jin, S., Park, P.H., Zhu, W., 2007. Micro-plate tectonics and kinematics in Northeast Asia inferred from a dense set of GPS observations. *Earth Planet. Sci. Lett.* 257, 486–496.
- Jo, N., Baag, C.-E., 2007. The 20 January 2007, M_w 4.5, Odaesan, Korea, earthquake. *Geosci. J.* 11, 51–58.
- June, M.S., 1990. Body-wave analysis for shallow intraplate earthquake in the Korean Peninsula and Yellow sea. *Tectonophysics* 192, 345–357.
- Kato, T., El-Fikey, G.S., Oware, E.N., Miyazaki, S., 1998. Crustal strains in the Japanese islands as deduced from dense GPS array. *Geophys. Res. Lett.* 25, 2445–2448.
- Kim, J.K., 2007. A study for earthquake parameter of Odaesan earthquake. *J. Eng. Geol.* 17 (4), 665–672.
- Kim, H.-K., Park, Y., 2010. The 20 January 2007 M_L 4.8 Odaesan earthquake and its implications for regional tectonics in Korea. *BSSA* 100 (3), 1395–1405.
- Kim, S.G., 1993. Seismological characteristics of the Korean Peninsula. *Continental Earthquakes*, vol. 3. Seismological Press, Beijing, China, pp. 130–141.
- Kim, S.G., Lkhasuren, E., Park, P.H., 2004. The low seismic activity of the Korean Peninsula surrounded by high earthquake countries. *J. Seismolog.* 8, 91–103.
- Kim, W.-Y., Choi, H., Noh, M., 2010. The 20 January 2007 Odaesan, Korea, earthquake sequence: reactivation of a buried strike-slip fault? *BSSA* 100 (3), 1120–1137.
- Kogan, M.G., Steblov, G.M., King, R.W., Herring, T.A., Frolov, D.L., Egorov, S.G., Levin, V.Y., Jones, A., 2000. Geodetic constrains on the rigidity and relative motion of Eurasian and North American. *Geophys. Res. Lett.* 27, 2041–2044.
- Koyama, J., 1985. Earthquake source time function from coherent and incoherent rupture. *Tectonophysics* 118, 227–242.
- Lawson, C.L., Hanson, R.J., 1974. *Solving Least Squares Problems*. Prentice-Hall, Englewood Cliffs, NJ. (340).
- Legrand, D., Delouis, B., 1999. Determination of the fault plane using single near field seismic station with a finite-dimension of source model. *Geophys. J. Int.* 138, 801–808.
- Li, Y., Doll Jr., C., Toksoz, M.N., 1995. Source characterization and fault plane determinations for $M = 1.2$ – 4.4 earthquakes in the Charlevoix seismic zone, Quebec, Canada. *Bull. Seismol. Soc. Am.* 85, 1604–1621.
- McGuire, J.J., 2004. Estimating finite source properties of small earthquake ruptures. *Bull. Seismol. Soc. Am.* 94, 377–393.
- Molnar, P., Tapponnier, P., 1975. Cenozoic tectonic of Asia: effects of a continental collision. *Science* 189, 419–426.
- Mori, J., 1996. Rupture directivity and slip distribution of the M 4.3 foreshock to the 1992 Joshua tree earthquake, southern California. *Bull. Seismol. Soc. Am.* 86, 805–810.
- Mori, J., Hartzell, S., 1990. Source inversion of the 1998 upland earthquake: determination of a fault plane for a small event. *Bull. Seismol. Soc. Am.* 80, 507–518.
- Mueller, C., 1985. Source pulse enhancement by deconvolution of an empirical Green's function. *Geophys. Res. Lett.* 12, 33–36.
- Nakahara, H., Nishimura, T., Sato, H., Ohtake, M., Kinoshita, S., Hamaguchi, H., 2002. Broadband source process of the 1998 Iwate prefecture, Japan, earthquake as revealed from inversion analyses of seismic waveforms and envelopes. *Bull. Seismol. Soc. Am.* 92, 1708–1720.
- Oh, C.W., Krishnan, S., Kim, S.W., Kwon, Y.W., 2006. Mangerite magmatism associated with a probable Late-Premian to Triassic Hongseong-Odesan collision belt in South Korea. *Gondwana Res.* 9, 95–105.
- Okada, T., Umino, N., Ito, Y., Matsuzawa, T., Hasegawa, A., Kamiyama, M., 2001. Source processes of 15 September 1999 M 5.0 Sendai, Northeastern Japan, Earthquake and its M 3.8 foreshock by waveform inversion. *Bull. Seismol. Soc. Am.* 91, 1607–1618.
- Okada, T., Matsuzawa, T., Hasegawa, A., 2003. Comparison of source areas of M 4.8 ± 0.1 repeating earthquakes off Kamaishi, NE Japan: are asperities persistent features? *EPSL* 213, 361–374.
- Örgülü, G., Aktar, M., 2001. Regional moment tensor inversion for strong aftershocks of the August 17, 1999 Izmit earthquake (M_w 7.4). *Geophys. Res. Lett.* 28, 371–374.
- Ozalaybey, S., Ergin, M., Aktar, M., Tapirdamaz, C., Bic men, F., Yörük, A., 2002. The 1999 Izmit earthquake sequence in Turkey: seismological and tectonic aspects. *Bull. Seismol. Soc. Am.* 92, 376–386.
- Papageorgiou, A.S., Aki, K., 1983. A specific barrier model for the quantitative description of inhomogeneous faulting and the prediction of strong ground motion. I: description of the model. *Bull. Seismol. Soc. Am.* 73, 693–722.
- Park, S.-C., Hahm, I.K., 2010. Rupture pattern of a moderate earthquake in Odaesan, Korea. *Geosci. J.* 14 (2), 191–200.
- Park, J.C., Kim, W., Chung, T.W., Baag, C.E., Ree, J.H., 2007. Focal mechanisms of recent earthquakes in the Southern Korean Peninsula. *Geophys. J. Int.* 169, 1103–1114.
- Sagong, H., Kwon, S.-T., Ree, J.-H., 2005. Mesozoic episodic magmatism in South Korea and its tectonic implication. *Tectonics* 24. <http://dx.doi.org/10.1029/2004TC001720> (TC5002).
- Tsumura, K., 1967. Determination of earthquake magnitude from total duration of oscillation. *Bull. Earthquake Res. Inst. Univ. Tokyo* 45, 7–18.
- Velasco, A.A., Ammon, C.J., Lay, T., 1994. Recent large earthquakes near Cape Mendocino and in the Gorda plate: broadband source time functions, fault orientations, and rupture complexities. *J. Geophys. Res.* 99, 711–728.
- Yamada, T., Mori, J.J., Ide, S., Kawakata, H., Iio, Y., Ogasawara, H., 2005. Radiation efficiency and apparent stress of small earthquakes in a South African gold mine. *J. geophys. Res.* 110, B01305. <http://dx.doi.org/10.1029/2004JB003221>.
- Yoo, H.J., Herrmann, R.B., Cho, K.H., Lee, K., 2007. Imaging the three-dimensional crust of the Korean peninsula by joint inversion of surface-wave dispersion and teleseismic receiver functions. *Bull. Seism. Soc. Am.* 97 (3), 1002–1011.
- Zahradnik, J., 2002. Modeling the Skyros island, Aegean Sea $M_w = 6.5$ earthquake of July 26, 2001. *Stud. Geophys. Geod.* 46, 753–771.
- Zahradnik, J., Janski, J., Papatsimpa, K., 2001. Focal mechanisms of weak earthquakes from amplitude spectra and polarities. *Pure Appl. Geophys.* 158, 647–665.
- Zahradnik, J., Jansky, J., Sokos, E., Serpentsidaki, A., Lyon-Caen, H., Papadimitriou, P., 2004. Modeling the M_L 4.7 mainshock of the February–July 2001 earthquake sequence in Aegion, Greece. *J. Seismolog.* 8, 247–257.
- Zonenshain, L.P., Savostin, L.A., 1981. Geodynamics of the Baikal rift zone and plate tectonics of Asia. *Tectonophysics* 76, 1–45.